





# Characterization of a time-resolved non-contact scanning diffuse optical imaging system exploiting fast-gated single-photon avalanche diode detection

Cite as: Rev. Sci. Instrum. **87**, 035118 (2016); <https://doi.org/10.1063/1.4944562>

Submitted: 10 December 2015 . Accepted: 08 March 2016 . Published Online: 24 March 2016

Laura Di Sieno, Heidrun Wabnitz , Antonio Pifferi , Mikhail Mazurenka , Yoko Hoshi, Alberto Dalla Mora , Davide Contini, Gianluca Boso, Wolfgang Becker, Fabrizio Martelli, Alberto Tosi , and Rainer Macdonald



View Online



Export Citation



CrossMark

## ARTICLES YOU MAY BE INTERESTED IN

[Time-resolved single-photon detection module based on silicon photomultiplier: A novel building block for time-correlated measurement systems](#)

Review of Scientific Instruments **87**, 073101 (2016); <https://doi.org/10.1063/1.4954968>

[MONSTIR II: A 32-channel, multispectral, time-resolved optical tomography system for neonatal brain imaging](#)

Review of Scientific Instruments **85**, 053105 (2014); <https://doi.org/10.1063/1.4875593>

[High-efficiency integrated readout circuit for single photon avalanche diode arrays in fluorescence lifetime imaging](#)

Review of Scientific Instruments **87**, 113110 (2016); <https://doi.org/10.1063/1.4968199>



**JANIS**

Janis Dilution Refrigerators & Helium-3 Cryostats  
for Sub-Kelvin SPM

Click here for more info [www.janis.com/UHV-ULT-SPM.aspx](http://www.janis.com/UHV-ULT-SPM.aspx)

# Characterization of a time-resolved non-contact scanning diffuse optical imaging system exploiting fast-gated single-photon avalanche diode detection

Laura Di Sieno,<sup>1,a)</sup> Heidrun Wabnitz,<sup>2</sup> Antonio Pifferi,<sup>1,3</sup> Mikhail Mazurenka,<sup>2,4</sup> Yoko Hoshi,<sup>5</sup> Alberto Dalla Mora,<sup>1</sup> Davide Contini,<sup>1</sup> Gianluca Boso,<sup>6,b)</sup> Wolfgang Becker,<sup>7</sup> Fabrizio Martelli,<sup>8</sup> Alberto Tosi,<sup>6</sup> and Rainer Macdonald<sup>2</sup>

<sup>1</sup>*Politecnico di Milano, Dipartimento di Fisica, Piazza Leonardo Da Vinci 32, 20133 Milano, Italy*

<sup>2</sup>*Physikalisch-Technische Bundesanstalt (PTB), Abbestr. 2-12, 10587 Berlin, Germany*

<sup>3</sup>*Istituto di Fotonica e Nanotecnologie, Consiglio Nazionale delle Ricerche, Piazza Leonardo da Vinci 32, 20133 Milano, Italy*

<sup>4</sup>*Hannoversches Zentrum für Optische Technologien, Nienburger Str. 17, 30167 Hannover, Germany*

<sup>5</sup>*Department of Biomedical Optics, Medical Photonics Research Center, Hamamatsu University School of Medicine, Hamamatsu 431-3192, Japan*

<sup>6</sup>*Politecnico di Milano, Dipartimento di Elettronica, Informazione e Bioingegneria, Piazza Leonardo Da Vinci 32, 20133 Milano, Italy*

<sup>7</sup>*Becker and Hickl GmbH, Nahmitzer Damm 30, 12277 Berlin, Germany*

<sup>8</sup>*Dipartimento di Fisica e Astronomia dell'Università degli Studi di Firenze, Via G. Sansone 1, Sesto Fiorentino, Firenze 50019, Italy*

(Received 10 December 2015; accepted 8 March 2016; published online 24 March 2016)

We present a system for non-contact time-resolved diffuse reflectance imaging, based on small source-detector distance and high dynamic range measurements utilizing a fast-gated single-photon avalanche diode. The system is suitable for imaging of diffusive media without any contact with the sample and with a spatial resolution of about 1 cm at 1 cm depth. In order to objectively assess its performances, we adopted two standardized protocols developed for time-domain brain imagers. The related tests included the recording of the instrument response function of the setup and the responsivity of its detection system. Moreover, by using liquid turbid phantoms with absorbing inclusions, depth-dependent contrast and contrast-to-noise ratio as well as lateral spatial resolution were measured. To illustrate the potentialities of the novel approach, the characteristics of the non-contact system are discussed and compared to those of a fiber-based brain imager. © 2016 Author(s). All article content, except where otherwise noted, is licensed under a Creative Commons Attribution (CC BY) license (<http://creativecommons.org/licenses/by/4.0/>). [<http://dx.doi.org/10.1063/1.4944562>]

## I. INTRODUCTION

Diffuse optical spectroscopy is an important tool for characterization of a great variety of diffusive media<sup>1</sup> such as biological tissues, fruits,<sup>2</sup> wood,<sup>3</sup> or chemical compounds. In the past few decades, great interest has been focused on the non-invasive recovery of information on tissue composition and morphology, which are of considerable usefulness for diagnostic purposes.<sup>4–8</sup> In the wavelength range from 600 nm to 1100 nm, tissues behave as weakly absorbing but highly scattering media and light can deeply penetrate: this enables to estimate the concentration of dominant absorbers in the biological tissue (like hemoglobin, water, and lipids). In recent years, various attempts have been worked out to use near-infrared spectroscopy (NIRS) in different clinical applications to obtain, for example, information about the oxygenation of blood in tissues<sup>9–13</sup> or for other diagnostics purposes.<sup>4–8</sup> In most cases, optical fibers are used to inject light into tissues and

to collect emerging photons. One of the main disadvantages of this approach is the difficulty to establish a proper contact between fiber and skin during the measurement. The physical contact and pressure can also cause pain to the patient and represents an issue in situations where the contact must be avoided (e.g., burn injuries or wounds). Moreover, the different pressure applied to the skin can also induce a variation in the water content thus modifying the reflection coefficient of the skin surface.<sup>14</sup> In addition, a non-contact approach allows one to study a patient without the need to attach an arrangement of optodes: this is a great advantage when it is difficult to treat the subject (e.g., babies). Non-contact NIRS approaches for *in vivo* applications were already proposed in Refs. 15 and 16 with CW detection and a source-detector distance of a few tens of millimeters.

It is worth noting that only a non-contact scheme enables a scanning approach in which source and detection spots are moved across the tissue surface. The size of the scanned area, the number of source-detector pairs (pixels in the image), and their separation are highly flexible. The spatial resolution is the highest if the source-detector distance is small (~mm).

In case of a short source-detector distance, the time-resolved approach is compulsory to obtain information from

<sup>a)</sup>Author to whom correspondence should be addressed. Electronic mail: [laura.disieno@polimi.it](mailto:laura.disieno@polimi.it).

<sup>b)</sup>Present address: Group of Applied Physics, University of Geneva, Geneva 1211, Switzerland.

the depth of a turbid medium. The depth information is encoded in the photon travelling times. Indeed, in reflectance geometry, photons that are collected within a few hundreds of picoseconds with respect to the time of injection of the laser pulse have travelled only in a superficial region, whereas after 1 ns depths greater than 1 cm can be explored.<sup>17,18</sup> It has also been demonstrated that by using a quasi-null source-detector distance, an improvement of spatial resolution and an increase in the amount of detected photons at all times are obtained.<sup>19</sup> The main disadvantage of this technique is the huge increase (with respect to larger source-detector distance) of the peak of early photons causing saturation of the detection electronics. To overcome this problem, we use a single-photon avalanche diode (SPAD) in fast-gated mode<sup>20</sup> to extract late photons by rejecting the peak of early ones. Coupling the fast-gated SPAD to a time-correlated single-photon counting (TCSPC) board and after appropriate post-processing analysis (see Ref. 21 for further details), we could reconstruct the whole distribution of times of flight (DTOF) with a dynamic range of up to 8 decades.<sup>21</sup>

In another previous work,<sup>22</sup> we have shown the first proof-of-principle of non-contact time-resolved diffuse reflectance measurements on phantoms using a quasi-null source-detector distance approach and a fast-gated SPAD. We then upgraded our setup to perform a fast scan of the area to be monitored and we demonstrated the feasibility of *in vivo* measurements, in particular, to detect functional brain activation.<sup>23,24</sup>

In this paper, we describe an instrument for non-contact scanning time-resolved diffuse optical imaging together with

its characterization following established standardized protocols for performance assessment of diffuse optics system. With respect to the setup presented in Ref. 23 where a first proof-of-principle of *in vivo* measurements was shown, the setup has been redesigned to improve performances in terms of signal quantity (overall light collection efficiency) and quality. Furthermore, a second detection arm was added to record the early photons in parallel to the late ones. The objective assessment of system performances with respect to brain imaging applications on the basis of standardized protocols permits to quantitatively compare the new technology to state-of-the-art fiber-based systems, and thus to evaluate the possible impact of this novel technology and to identify future research directions.

This paper is organized as follows: Section II deals with the design of the instrumental setup. The experiments and the data analysis will be described in Section III while in Section IV results of the characterization of the setup will be presented. In Section V, the performances of the non-contact scanning setup and of a fiber-based brain imager will be compared. Finally, conclusions and future perspectives will be discussed in Section VI.

## II. SYSTEM ARCHITECTURE

### A. Laser source

The overall schematic of the system setup is depicted in Figure 1. As a light source, we used a picosecond

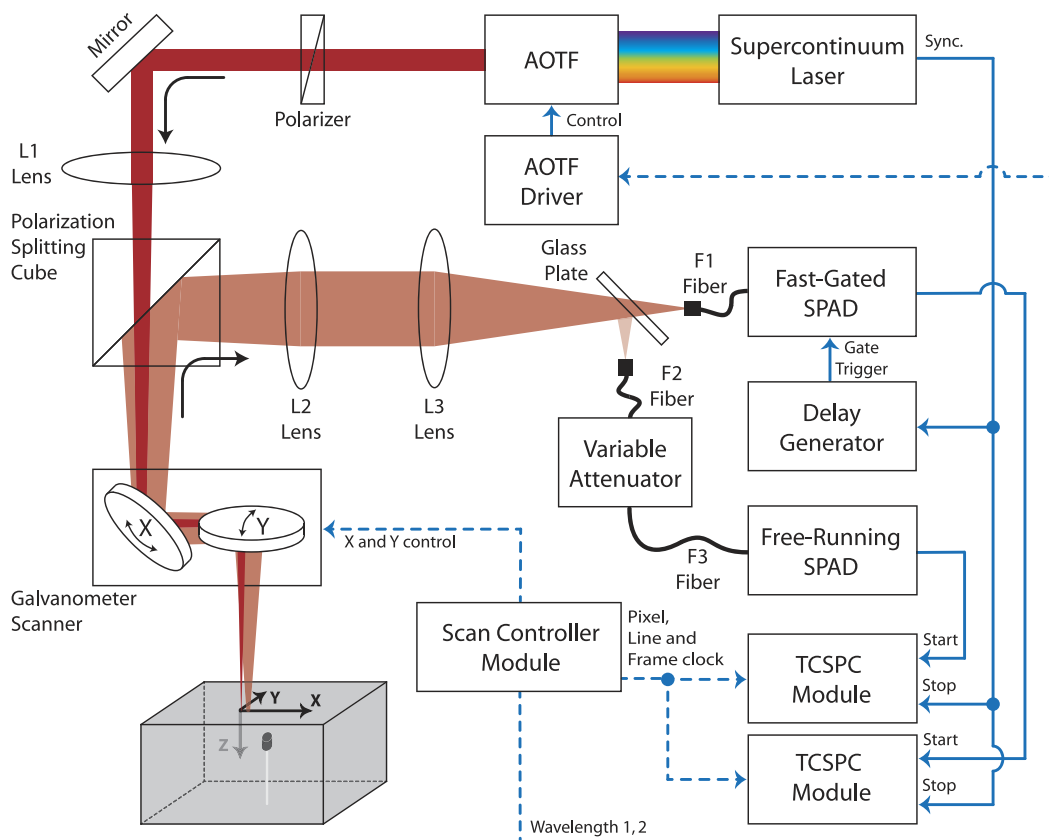


FIG. 1. Schematic of the setup.

supercontinuum laser (SC500-6, Fianium Ltd., United Kingdom) with a repetition rate of 40.5 MHz. It was equipped with an 8-channel acousto-optical tunable filter (AOTF) for the near-infrared (NIR) range (650 nm to 1100 nm). The 8 AOTF channels were activated simultaneously with a small spectral offset ( $\sim 4$  nm between adjacent channels) so as to increase the laser power injected into the sample at the expense of increasing the overall spectral width. Further, we exploited the capability of fast switching ( $< 3 \mu\text{s}$ )<sup>24</sup> between two different wavelengths, simultaneously for all channels, for rapidly alternating between two wavelength ranges. As a result, we obtained an effective source operated alternately at the two central wavelengths of 760 nm and 860 nm with a bandwidth of around 30 nm and an average power of  $\sim 30$  mW each. These two wavelength ranges were chosen such that they were appropriate for *in vivo* measurements (namely, for the calculation of the concentration changes of oxygenated and deoxygenated hemoglobin, according to the algorithm described in Ref. 23) and contained comparable output power. The “pulse train monitor” output of the laser was utilized as *sync* signal to derive the “stop” pulses for the TCSPC recording as well as the gate trigger for the fast-gated detector (for further details see Subsection II C).

## B. Optics

Linearly polarized light exiting the laser passed through the lens L1 ( $f = 300$  mm, Thorlabs GmbH, Germany), a polarization splitting cube for the NIR range, with 50 mm dimension (Edmund Optics GmbH, Germany) and hit the sample to be measured. The size of the spot on the sample can be enlarged by moving lens L1 along its axis so as to comply with safety requirements in case the system is used *in vivo*. The polarization splitting cube was used to efficiently suppress the directly reflected or single scattered light while transmitting half of the diffusely scattered unpolarized light returning from the sample.<sup>25</sup> Thus, photons exiting from the sample with a polarization state orthogonal with respect to the incident light were redirected towards lenses L2 and L3 ( $f = 300$  mm and  $f = 125$  mm, respectively, Thorlabs GmbH, Germany). We used 2-in. diameter lenses and a 2-in. polarization splitting cube, thus enlarging the numerical aperture (NA) of the system, to achieve a high light harvesting efficiency. By slightly changing the direction of the focused input beam, the laser spot on the sample could be offset relative to the spot from which the light is detected by an adjustable distance (source-detector distance). Because of an afterpulse-like effect known as “memory effect”<sup>26</sup> that increases the background level when high light intensities hit the gated SPAD detector at times outside the gate, it was preferable to work at small (a few mm) rather than zero source-detector distance, to reduce the amount of early photons arriving at the detector to some extent.

A glass plate was introduced between lens L3 and detection fiber F1 ( $\text{Ø}200 \mu\text{m}$ , 0.48 NA, 2 m long, CeramOptec GmbH, Germany) to reflect a small fraction of the collected photons into the “early photon” arm of the detection system. The light transmitted through the glass plate was then sent into fiber F1 that had an entrance face angled by  $8^\circ$  to prevent

light from being reflected back into the optical path. The output face of F1 was imaged onto the active area (diameter  $100 \mu\text{m}$ ) of the fast-gated silicon SPAD (that recorded late photons) by means of a demagnifying telescope made of a pair of aspheric lenses. The early photons arm consisted of the fibers F2 ( $\text{Ø}600 \mu\text{m}$ , 0.39 NA, 2 m long, Thorlabs GmbH, Germany) and F3 (pigtailed graded-index fiber,  $\text{Ø}62.5 \mu\text{m}$ ) which delivered the light to a silicon SPAD (Micro Photon Device S.r.l., Italy) operated in free-running mode. In order to adjust the count rate, a variable attenuator (VA) was inserted between the fibers F2 and F3, both equipped with collimating optics.

The illumination spot size was small compared to 1 mm. The size of the detection spot was estimated by coupling light into the far end of the detection fiber and analyzing the illuminated spot in the sample plane. The spot size for the late photon detection arm was about 1 mm, i.e., both spot sizes were small compared to the source-detector separation of 5 mm. Due to the larger fiber diameter in the early photon detection arm, its detection area was about 3 times larger. This difference was not relevant for the measurement.

The distance between scan head and sample was 130 mm. In case of an application on the human head, its curvature would introduce a varying distance from the scanner. The major effect would be a time shift related to the time needed for the light to travel twice the difference in distance. The DTOF would be shifted with respect to the gate. This shift can be calculated by determining the temporal position of the non-gated DTOF recorded with the early photon channel. For correction, the time windows selected for analysis need to be shifted accordingly.

## C. Fast-gated SPAD module

A second generation compact fast-gated SPAD module with embedded gating and signal conditioning circuitry<sup>20</sup> was employed for selective detection of late photons. The fast-gated SPAD module was conceived and developed by Dipartimento di Elettronica, Informazione e Bioingegneria of Politecnico di Milano. The active area of the silicon SPAD had a diameter of  $100 \mu\text{m}$ . A mixed-signal amplifier comprising ECL (emitter-coupled logic) and microwave components allowed to achieve turn-ON and turn-OFF transition times below 200 ps and gating windows from 10 ns down to just few hundreds of picoseconds, at repetition rates up to 50 MHz. A differential front-end electronics read out the avalanche current pulse while rejecting spurious spikes due to the gate pulse, thus achieving a photon detection timing jitter below 30 ps. In the experiments reported here, the gate duration was set to 6 ns and the gate delay was adjusted by a home-built transmission-line based delay generator with 25 ps steps. A delay of about 1.3 ns with respect to the early photon peak was typically chosen in the *in vivo* experiments.<sup>23</sup> This delay still allowed a maximum count rate of  $3 \times 10^6 \text{ s}^{-1}$  to be achieved for late photons, to maintain a high signal-to-noise ratio (SNR). When a photon causes an avalanche within the detector, a low-jitter standard nuclear instrumentation module (NIM) pulse is provided by the high-speed comparator of the SPAD module and is fed to the “start” input of the TCSPC module. Both the TCSPC



sync signal (“stop”) and the gate trigger were derived from the pulse train of the supercontinuum laser.

We note that at high count rates the influence of the pileup effect in photon counting needs to be considered. Part of the single photon pulses remains undetected due to the dead time of the detector or the electronic processing. Since our analysis does not explicitly rely on the shape of the DTOF and the dead time is much larger than the pulse period, the overall counting loss is more relevant than a distortion of the temporal profile. The effect of the counting loss can be estimated according to Refs. 27 and 28. Since the dead time of the SPC-150 modules is as short as about 100 ns, the counting loss at  $3 \times 10^6 \text{ s}^{-1}$  amounts to 30% which may still be tolerable.

#### D. Data acquisition

Two separate detection channels were employed to record the DTOFs from both detectors, i.e., late photons were detected by the time-gated SPAD module and the complete DTOF (including early photons) was obtained by the free-running SPAD.

Scanning control and image acquisition were performed by a combination of a GVD-120 scan controller and two SPC-150 TCSPC modules (both Becker & Hickl, Germany).<sup>27</sup> The GVD-120 card runs a raster scan, generates X and Y (analog) signals for the galvanometer scanner, and controls one or two lasers. Synchronization with the image acquisition in the TCSPC module is performed via “Pixel Clock,” “Line Clock,” and “Frame Clock” pulses as described in Ref. 27. In each SPC-150 module, the recording process builds up a three-dimensional photon distribution over the scan coordinates and the arrival times of the photons within the laser pulse period. The result is an array of pixels, each containing the waveform of the optical signal.

The recording in the SPC-150 modules was run in the “Scan Sync In” (hardware acquisition) mode combined with “continuous flow” recording. In this mode, the device memory is divided into two memory banks. The recording system writes new data into one bank while previous data are read from the other bank and written to the hard disk. When the current image is completed, the memory banks are swapped and the procedure continues. In this way, a virtually unlimited time series of contiguous recordings is obtained.<sup>27</sup>

System parameters, such as operation modes, pixel numbers, scan amplitudes, aspect ratio of the scan, multiplexing mode, number of time channels, or width of the time channels, were defined via single photon counting module data acquisition software (Becker & Hickl, Germany).

Two laser wavelengths were multiplexed on a line-by-line basis via the AOTF of the supercontinuum laser, making use of the “FSK” (Frequency Shift Keying) mode of the AOTF. Multiplexing was controlled via the laser multiplexing function of the GVD-120 scan controller card. The FSK input signal was derived from its “laser routing” outputs. This way, odd lines and even lines of the scan were run with wavelengths of 860 nm and 760 nm, respectively.

With a total of  $32 \times 32$  pixels per frame, two  $32 \times 16$  pixel images corresponding to the two wavelengths were recorded

quasi-simultaneously. The DTOFs in the individual pixels (1024 per frame of the scan) were collected into 1024 time channels of 12 ps width.

### III. EXPERIMENTS AND ANALYSIS

In order to characterize the setup, we adopted two standardized protocols for performance assessment of time-domain optical brain imagers: the Basic Instrumental Performance protocol<sup>29</sup> and the nEUROpt protocol,<sup>30</sup> in particular, the tests related to the Instrument Response Function (IRF) and the responsivity of the detection system (part of the BIP protocol) as well as several tests of the nEUROpt protocol related to contrast, contrast-to-noise ratio, and lateral spatial resolution. In the following, the various types of experiments performed on the non-contact setup and the related data analysis will be detailed.

#### A. Recording of the IRF

The IRF characterizes the temporal resolution of a time-resolved measuring system as a whole. It depends on the temporal profile of the laser pulse, the temporal response of the detector and electronics, and pulse broadening due to temporal dispersion in the fiber-optic components. It is measured with a reference sample that does not contribute any additional temporal dispersion. In case of a gated detector, such recording depends on the gate parameters. In the context of the present paper, we define the IRF in a slightly different manner, i.e., by synthesizing an overall response based on many recordings at different gate delays. The IRF obtained in this way from gated measurements is particularly useful since it allows to estimate the overall dynamic range of the acquisition system and the influence of reflections on the measurements. Such synthetic IRF is also relevant for simulations of the system behavior. To obtain this complete IRF with a high dynamic range, we exploited the technique proposed in Ref. 21. As reference sample with negligible temporal dispersion, we used a small piece of white paper. The injection and detection spots were overlapped (zero source-detector distance). We acquired subsequent portions of the IRF at increasing delays (with steps of 25 ps) and with increasing incident power while keeping the count rate at a level of about  $10^6 \text{ s}^{-1}$ . The injected power was increased by means of a variable attenuator (not shown in Figure 1) inserted in the laser beam. The collection time in each step was 10 s.

The resulting curves were rescaled by the values of attenuation introduced and a high dynamic range curve was reconstructed after eliminating the region around the leading edge of the gate as well as the noisy tail for each piece. Before that, the constant background (representing the dark count rate) was subtracted from all measurements. Its value was obtained in an initial measurement without clipping the curve by the gate. An additional background component due to the “memory effect”<sup>26,31</sup> is related to the total amount of light impinging on the detector when it is off and thus increases with increasing delay. Therefore it cannot be subtracted as a constant background but should remain part

of the reconstructed IRF thus limiting the achievable dynamic range.

## B. Responsivity measurement

In the context of the BIP protocol,<sup>29</sup> the responsivity quantifies the overall efficiency of the detection system (including the detector and the optics between sample and detector), to detect light diffusely emerging from tissue. It was defined as the ratio between the measured count rate  $N_{\text{det}}$  and the input photon radiance. Dedicated solid slab phantoms were used to provide a known input radiance with a nearly Lambertian angular distribution. With the known wavelength-dependent photon transmittance factor  $\kappa_p$  of the phantom and the average laser power  $P_{\text{in}}$  impinging on the phantom, the spectral responsivity of the detection system with respect to photon radiance is calculated as follows:

$$S_{\text{det}}^L(\lambda) = N_{\text{det}} / [\kappa_p(\lambda) P_{\text{in}}(\lambda)]. \quad (1)$$

The unit of  $S_{\text{det}}^L(\lambda)$  is  $\text{m}^2 \text{sr}$ . For further details, see Ref. 29.

The responsivity measurement on the non-contact system was performed as follows. The laser light was focused into a multimode fiber.  $P_{\text{in}}$  was measured at the exit face of the fiber. The fiber was then mounted in the center of the entrance face of the responsivity phantom, in contact with its surface. The exit face of the phantom was positioned in the sample plane of the non-contact system and its center was adjusted to coincide with the detection spot (with fixed X and Y positions) before a non-gated DTOF was recorded. The count rate was obtained from the time-integrated total photon count divided by the measurement time.

## C. Measurements on a liquid phantom with localized absorber

To assess sensitivity and spatial resolution of a localized absorption change (that can simulate the localized variation in optical properties due to hemodynamic response of the brain), heterogeneous tissue phantoms are required. The nEUROPt protocol<sup>30</sup> proposed, in particular, the use of a liquid turbid phantom with five small solid black inclusions of various size. As explained in Ref. 32, a totally absorbing object of the proper volume can mimic the effect of an absorption perturbation of any value and volume within a large range of validity. The key situation when this equivalence is violated is for shallow (e.g., <5–10 mm) depths of the black inclusion. However, even in this occurrence, the test is still useful to compare the performances of different instruments under the same conditions.

The liquid phantom was based on a water dilution of Intralipid-20% as diffusive medium and India ink as absorber poured in a transparent plastic tank. The dimensions of the liquid volume were  $21 \times 16 \times 10 \text{ cm}^3$  with 10 cm in Z direction, large enough to be regarded as a semi-infinite medium. Both the reduced scattering and absorption coefficients for Intralipid and the absorption coefficient for ink have been extensively characterized with different techniques (continuous wave<sup>33,34</sup> and time-resolved<sup>35</sup>), and finally reference values derived from a multi-laboratory study

were adopted.<sup>36</sup> From the amounts of Intralipid and diluted ink mixed with water, the resulting optical properties were estimated: a reduced scattering coefficient ( $\mu'_s$ ) of  $8.4 \text{ cm}^{-1}$  and  $7.2 \text{ cm}^{-1}$  and an absorption coefficient ( $\mu_a$ ) of  $0.11 \text{ cm}^{-1}$  and  $0.12 \text{ cm}^{-1}$  for 760 nm and 860 nm, respectively.

To simulate the presence of a localized absorption perturbation, we used five black plastic (polyvinyl chloride, PVC) cylinders (height equal to diameter whose values were 3.2, 4, 5, 6.8, and 8.6 mm) of different volumes (25, 50, 100, 250, and 500  $\text{mm}^3$ , respectively).<sup>37</sup> They were held in the liquid in upright position, supported by a rigid wire from underneath. The Z value refers to the distance between the upper (circular) face of the cylinder and the surface of the liquid.

The scan images of the liquid phantom were acquired with a frame rate (i.e., the number of full images acquired per second) of  $1 \text{ s}^{-1}$ . For each Z position of the inclusion, 100 frames were recorded and stored. Each image contained  $32 \times 32$  pixels covering an area of  $34 \times 40 \text{ mm}^2$ , with line-by-line interlacing of wavelengths. The scan area was centered at the position of the inclusion. The offset between illumination and detection spots (source-detector distance) was adjusted to 5 mm in X direction.

## D. Data analysis of scan images

We first separated the images of DTOFs for the two wavelengths, thus obtaining two images of  $32 \times 16$  pixels. Each image was then binned along rows (Y direction, bin factor: 2) to have square images of  $16 \times 16$  pixels before time-windowing of the curves. Prior to further analysis, we subtracted the constant background from each DTOF.

We then computed contrast, contrast-to-noise ratio, and lateral spatial resolution as defined in the nEUROPt protocol.<sup>30</sup> For both detection channels, the contrast was calculated based on the total photon count within selected time windows ( $t_w$ ) of the DTOFs for each pixel ( $m, n$ ) using the following equation:

$$C(t_w)^{(m,n)}_Z = \frac{N(t_w)^{(m,n)}_Z - N_0(t_w)_Z}{N_0(t_w)_Z} \quad (2)$$

in which  $N_0$  is the number of photons collected in the unperturbed, homogeneous case (source and detector far from the inclusion) while  $N$  is the count with the perturbation present. This calculation was performed for all depths Z of the inclusion. It should be noted that the contrast definition in Eq. (2) is a relative contrast (the difference is normalized to the unperturbed value) for which the absolute photon count is irrelevant.

For early photons, the width of the time window was set equal to 1.4 ns in order to integrate essentially the whole DTOF. Since in the “early photon” detection arm of the setup the SPAD detector is not gated, the whole DTOF at a short source-detector distance is dominated by the peak of early photons.

For late photons, we selected a window 960 ps long and delayed by 1.54 ns with respect to the maximum of the DTOF recorded with the same detector configuration but without clipping by the gate (i.e., gate opened before the first re-emitted photons are recorded). Indeed, it was opened 1.15 ns after the

peak of the DTOF and the portion of the curve analyzed started 391 ps after the rising edge of the gate.

The position and the width of the time window were chosen such that a sufficient count of late photons was collected and that the region of the curve contaminated by optical reflections which could affect the contrast was avoided. For contrast and spatial resolution features, counts accumulated within the same time window were summed up over all (93) frames recorded (each frame: 1 s of collection time) in order to increase the signal-to-noise ratio.

According to Ref. 30, lateral resolution was computed for the 100 mm<sup>3</sup> inclusion at 10 mm depth, in the pixel (8,8) where the maximum relative contrast (computed as previously stated) was recorded. The lateral resolution is defined as the full width at half maximum (FWHM) of the contrast curve *vs.* the lateral coordinate in the direction under test.

For contrast-to-noise ratio (CNR), we made use of the definition given in<sup>30</sup>

$$CNR = \frac{\Delta N(t_w)}{\sigma(N_0(t_w))} = \frac{N_0(t_w) - N(t_w)}{\sigma(N_0(t_w))}. \quad (3)$$

This definition is not meant for an image but for a single point acquisition. For this reason, there is no reference to pixel. However, for the analysis of scan images, the meaning of the terms appearing in (3) was modified as described in the following.  $\Delta N$  was taken as the mean value (over all frames) of the difference  $N_0(t_w) - N(t_w)$  at the location of maximum contrast, for the time window under consideration. The denominator  $\sigma(N_0(t_w))$  was computed as the standard deviation (over all frames) of the counts summed over a reference region (area: 3 × 3 pixels of the 16 × 16 pixel image) where the influence of the inclusion was negligible. It should be noted that the standard deviation and thus the CNR calculated in this way refer to an effective collection time of 18 ms, taking into account any binning of pixels.

Examples of contrast images of the phantom are shown in Figure 2, with the cylinder of 100 mm<sup>3</sup> positioned at increasing depths *Z*, obtained with both early (collected with the non-gated SPAD, first row) and late photons (detected by means of the fast-gated SPAD, second row). As expected, when using

late photons, the presence of the inclusion can be revealed up to considerably larger depths. The images for *Z* = 0 mm for both early and late channels (first column in Figure 2) show the contrast in the central pixels to be approximately 1. At this shallow depth (i.e., the inclusion just below the source and detector spot, covered by a very thin layer of liquid only), most of the photons are absorbed by the black inclusion itself: for this reason, very few photons  $N(t_w)_z^{(m,n)}$  return and can be collected by the detection optics. This amount is nearly negligible if compared to  $N_0(t_w)_z^{(m,n)}$ , and thus the contrast approaches 1. The rigorous characterization of the performances of the setup will be detailed in the following paragraph.

#### IV. PERFORMANCE ASSESSMENT

First the results of the IRF and responsivity tests for the “late-photon” detection arm of the non-contact setup that contains the fast-gated SPAD will be discussed. Figure 3 presents the IRF for both wavelengths. The dynamic range is about 7 decades. Peaks in the tail of the curve are caused by incompletely suppressed reflections in the optical path. It should be noted that the tremendous dynamic range of the gated approach makes it particularly sensitive to optical reflections. Very small fractions of the peak of early photons reflected or scattered into the detector with a delay in the late-photon range become noticeable. Even higher-order reflections at optical elements, e.g., fiber tips can be detected. This represents a problem because reflections both distort the time resolved-curve and can saturate the measurements for the highest delays during gated acquisitions. However, by knowing their temporal position, the origin of such reflections in the optical path can be traced back and measures can be taken to minimize them.

For what concerns temporal resolution, the FWHM of the IRF was 52 ps and 58 ps for 760 and 860 nm, respectively. The time constant of the diffusion tail of the fast-gated SPAD was estimated as 85 ps (see Ref. 38).

The responsivity of the detection system containing the fast-gated SPAD was determined as  $3.9 \times 10^{-5}$  and  $1.8 \times 10^{-5}$  mm<sup>2</sup> sr for 760 and 860 nm, respectively. The smaller

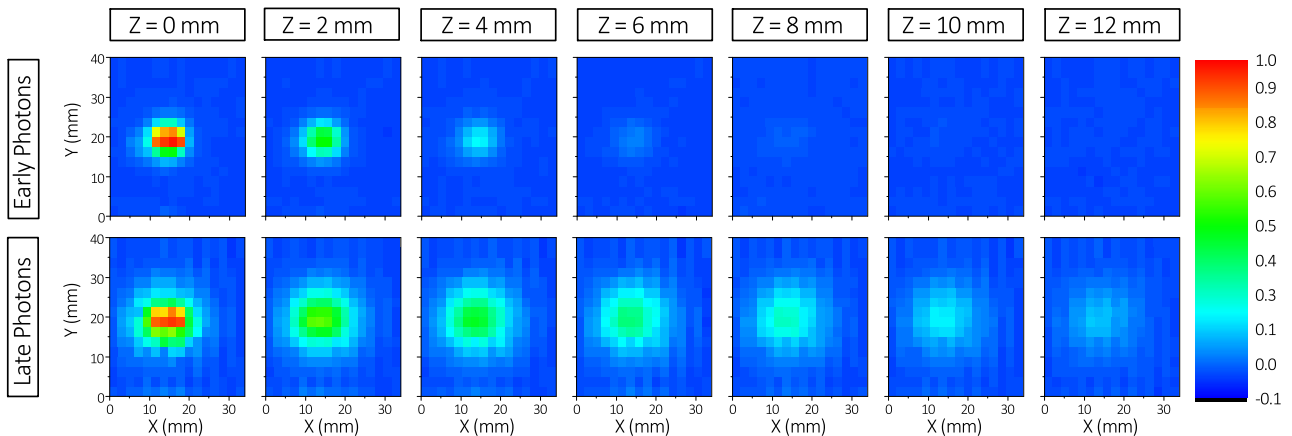


FIG. 2. Example of maps of contrast computed exploiting early (first row of panels) and late (second row) photons for different depths (*Z*) of the black cylinder of 100 mm<sup>3</sup> volume (columns). For *Z* = 0 the upper face of the cylinder is flush with the surface of the liquid.

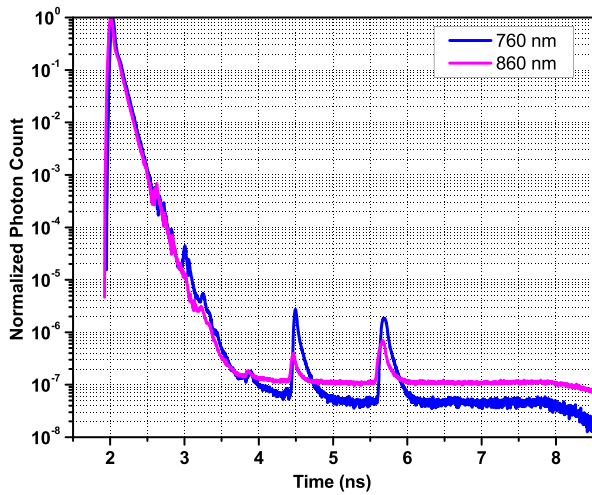


FIG. 3. IRF for the fast-gated detector in the non-contact setup at both wavelengths.

value at the 860 nm can be attributed to the wavelength dependence of the SPAD quantum efficiency, which is nearly 20% and 9% for 760 nm and 860 nm, respectively.<sup>39</sup> Indeed, it can be verified that the ratio between the responsivities

at the two wavelengths is the same as the ratio of the quantum efficiencies. The magnitude of the responsivity will be discussed in more detail in Sec. V.

The results of several tests (performed for the 100 mm<sup>3</sup> inclusion, as reported in Ref. 30) according to the nEUROpt protocol assessing contrast, contrast-to-noise, and lateral resolution (in X and Y directions) are presented in Figure 4. They were obtained from two-dimensional images as those shown in Figure 2. To locate the central position for each inclusion, the pixel with maximum contrast was identified in the image for Z = 0. For the lateral resolution, lines through this pixel in X and Y directions were analyzed, as explained in Sec. III. In the upper left panel (Figure 4(a)), the contrast computed for early as well as late photons is displayed.

As expected from theory and simulations,<sup>19</sup> the contrast computed using the later part of the DTOF is higher for any depth of the inclusion than for early photons, except for the most superficial positions that are also reached by early photons. With late photons, it is possible to see a totally absorbing inclusion of 100 mm<sup>3</sup> volume inclusion (equivalent to  $\Delta\mu_a = 0.15 \text{ cm}^{-1}$  within a spherical volume  $V_0 = 1000 \text{ mm}^3$ ) up to a depth of 14 mm where the contrast

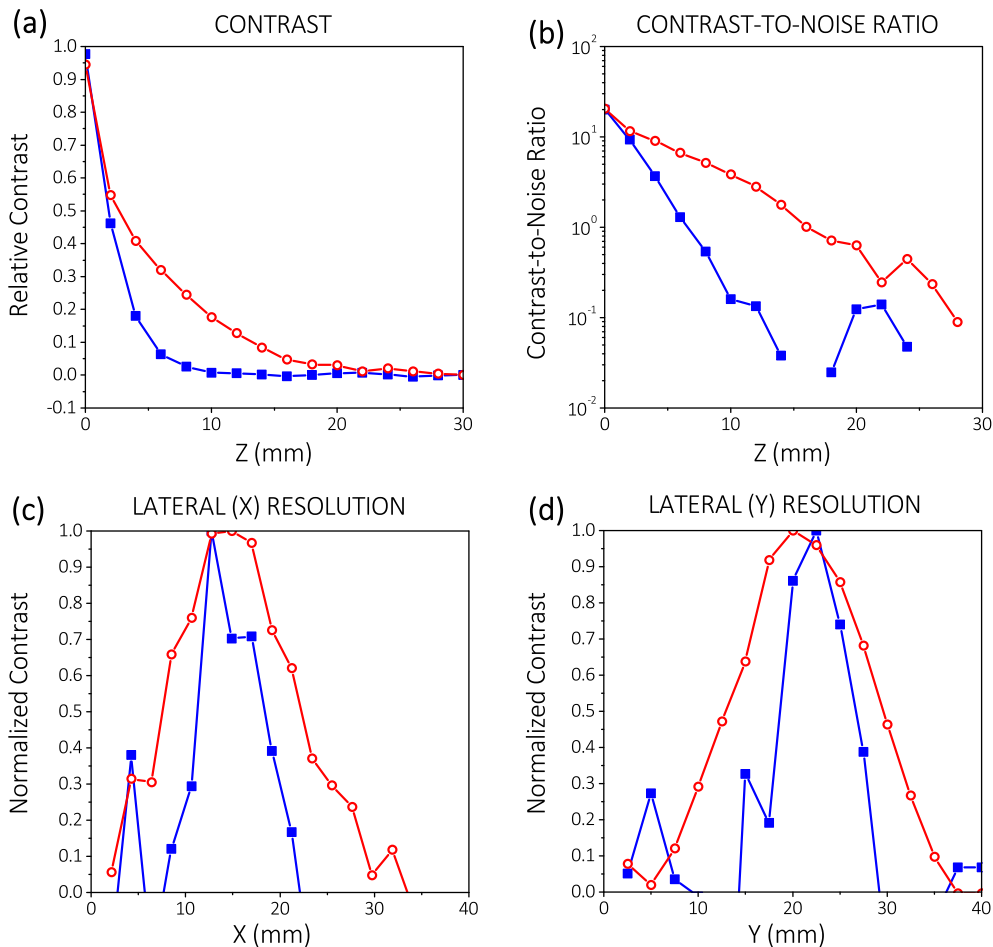


FIG. 4. Results of tests of the non-contact system according to the nEUROpt protocol:<sup>30</sup> depth-dependent contrast (a) and contrast-to-noise ratio (b), lateral resolution in X and Y directions (c) and (d) measured for early photons (non-gated detector, filled squares) and a late time window (recorded with the gated detector, open circles) for pixel (8,8) in both cases. Measurements for (a)-(d) with black cylinder of 100 mm<sup>3</sup> volume; depth for (c) and (d) Z = 10 mm. Please note that in graph (b), for early photons, the point at 16 mm depth is missing because it had a negative value.



is still nearly 0.05 and the CNR is large enough (1.77, see Figure 4(b)) to notice the presence of a perturbation while for early photons the inclusion can only be properly detected at shallow depths.

It should be noted that the contrast may be slightly underestimated due to the pileup effect which was mentioned above in Section II C. To mimic the conditions of *in vivo* experiments, the phantom experiments were performed in the gated detection channel at about  $2.2 \times 10^6 \text{ s}^{-1}$ . The corresponding counting loss can be estimated as 22%. It can be shown that this counting loss leads to a reduction in contrast (according to the definition in Eq. (2)) of 22% likewise, for small contrast. For larger contrast values, the relative contrast reduction decreases and approaches 0 at contrast 1.

Figures 4(c) and 4(d) represent X and Y resolutions, respectively, for a fixed depth (10 mm). As can be inferred from Figure 4(b), for early photons, the CNR at 10 mm is about 0.2 only. Thus the shape of the lateral profiles is noisy and not well defined. For late photons, a still rather low CNR (whose value is 4.5) is also responsible for the somewhat noisy profile of the X resolution graph.

In this case, however, it is possible to recover the FWHM of the lateral resolution whose value is 16 mm and 15 mm for X and Y directions, respectively. Notwithstanding the noisy lateral resolution profiles obtained for early photons, it is clearly noticeable that the FWHM in this case is smaller than the one achievable using late photons. This consideration is in perfect agreement with theory since early photons are scarcely diffused and so they probe a more confined and more superficial region thus resulting in an improved spatial resolution but in a negligible contrast for depths larger than a few millimeters.

## V. COMPARISON WITH A FIBER-BASED OPTICAL BRAIN IMAGER

Table I presents the synthetic descriptors summarizing the key performances related to the various tests of the BIP and nEUROPt protocols for the present setup (“non-contact system”) in comparison with those for the clinical fiber-based time-domain prototype “fOXY” developed by Politecnico di Milano and described in Refs. 40 and 41. We choose this prototype as a typical time-domain optical brain imager for

which the results of the tests of both the BIP and nEUROPt protocols were already published.<sup>29,30</sup>

For the BIP parameters, we can see that the responsivity computed for the non-contact setup is nearly by 3 decades lower than that of fOXY. This loss in photon detection efficiency can be easily explained by several factors: (1) the active area of the fast-gated SPAD detector is smaller by about a factor of 300 compared to that of photomultipliers (PMTs) (R5900-20-M4, Hamamatsu Photonics, Japan) used in fOXY; (2) the acceptance angle in which photons from the turbid sample are collected and sent to the fiber F1 (see Figure 1) is much smaller than in case of light collection by an optical fiber bundle of high numerical aperture directly attached to the tissue; and (3) the coupling of the photons coming from the fiber onto the SPAD was not perfect. In addition, it should be noted that it is not easy to fulfill altogether the following conditions: a demagnification of the image of the output face of the fiber F1 onto the detector, the transfer of a wide angular distribution of light exiting F1, and a not too short working distance of the telescope. The minimum working distance of the focusing optics was limited by the presence of bond wires around the SPAD chip integrated in a printed circuit board. On the opposite in fOXY a better coupling between fiber bundle and detector is guaranteed.

On the other hand, the higher detection efficiency of the silicon SPAD (nearly 20% and 9% for 760 nm and 860 nm, respectively) with respect to the PMT cathode (nearly 2% at 690 nm<sup>42</sup>) partially compensates for the previous losses. In addition, the effect of the low responsivity of the detection system is further compensated by the opportunity to increase the injected laser power for large gate delays, thus providing a comparably high SNR for late photons.

For what concerns the temporal resolution, the SPAD-based scanning setup shows clearly improved performances: indeed, it has a lower FWHM of the IRF (nearly 8 times smaller) than fOXY (i.e., 52 ps and 450 ps, respectively). The following factors are relevant to explain this difference: the picosecond laser diodes had a considerably larger pulse width than the supercontinuum laser, and the long fiber bundles of high NA introduced substantial temporal dispersion.

The relative contrast due to an inclusion ( $V = 100 \text{ mm}^3$ ) positioned at 15 mm depth is smaller for the non-contact setup (8.7% vs. 17.2% obtained with fOXY). The contrast depends

TABLE I. Comparison between the non-contact scanning system based on a fast-gated SPAD detector and a fiber-based time-domain optical brain imager (“fOXY,” results for the nEUROPt protocol were taken from the report shown in Fig. 8 of Ref. 30).

Protocol	Test	Non-contact system <sup>a</sup>	fOXY <sup>b</sup>	Notes
BIP	Responsivity	$3.9 \times 10^{-5} \text{ mm}^2 \text{ sr}$	$4 \times 10^{-2} \text{ mm}^2 \text{ sr}$	For fOXY, responsivity taken at 690 nm
BIP	IRF: temporal resolution	52 ps	450 ps	
BIP	IRF: dynamic range	7 decades	4 decades	
nEUROPt	Relative contrast	0.087	0.172	For $z = 15 \text{ mm}$ . Contrast computed using different time windows
nEUROPt	CNR	4 (29.8 <sup>c</sup> )	18.4	For $z = 10 \text{ mm}$
nEUROPt	X resolution	16 mm	32 mm	For $z = 10 \text{ mm}$ ; FWHM
nEUROPt	Y resolution	15 mm	16 mm	For $z = 10 \text{ mm}$ ; FWHM

<sup>a</sup>Characterization done at 760 nm (optical properties of the phantom:  $\mu_a = 0.11 \text{ cm}^{-1}$ ;  $\mu'_s = 8.4 \text{ cm}^{-1}$ ). Time window used: 1.54 ns to 2.5 ns. Source-detector distance: 5 mm.

<sup>b</sup>Characterization done at 830 nm (optical properties of the phantom:  $\mu_a = 0.12 \text{ cm}^{-1}$ ;  $\mu'_s = 9.08 \text{ cm}^{-1}$ ). Time window used: 2.5 ns–3 ns. Source-detector distance: 30 mm.

<sup>c</sup>Value computed considering 1 s acquisition time without any scanning.

on the temporal position of the time window. At a fixed time, the contrast for the short source-detector distance of the non-contact system (5 mm) is theoretically expected to be equal or better than at the larger one of fOXY (30 mm).<sup>43</sup> However, the time windows employed in both systems were different; in case of the non-contact system, it started by about 1 ns earlier. The much lower responsivity of the system limited the maximum delay that could be reached in the non-contact setup. Having said that, the gated approach is indispensable to achieve a reasonable contrast for a deep inclusion at such short source-detector distance.

For what concerns the CNR, if analyzing this parameter following Eq. (3) (and reported in Figure 4) for the non-contact setup it is nearly 4.5 times smaller than what was reported for fOXY. This discrepancy is mainly due to the different acquisition times. Indeed, for the non-contact scanning setup, we analyzed data acquired in 18 pixels (total acquisition time of 18 ms) while in the other case measurements lasted 1 s, thus demoting the CNR of the non-contact setup. In order to have a fair comparison, we have to refer to the definition reported in Ref. 30 also for the non-contact setup. Hence the value of CNR has to be multiplied by a factor of  $\sqrt{(1\text{ s})/(18\text{ ms})} = 7.45$ .

As reported in Table I, the CNR computed for a single point with 1 s acquisition time is nearly 1.5 higher for the non-contact setup with respect to what is achievable with fOXY. This advantage of the gated approach can be understood in the following way. The count rates in both experiments were similar, but in case of the gated detector, this count rate refers to a late part of the DTOF only while in the fOXY measurement it contains the whole DTOF for the non-gated measurement at a large source-detector distance. Thus for equal acquisition time the photon noise  $\frac{\Delta N}{N} = \frac{1}{\sqrt{N}}$  for a fixed late time window can be expected to be lower in the gated case.

To assess the results of this comparison, it has to be noticed that the two setups under test have different aims: indeed, fOXY is a system that enables only a very rough localization of inhomogeneities (e.g., change in absorption coefficient due to brain activation) by an array of only a few tens of source-detector pairs (separation 3 cm) that are sparsely located covering an area of nearly  $10 \times 10\text{ cm}^2$ . On the other hand, the non-contact setup aims at fast scanning an area of nearly  $4 \times 4\text{ cm}^2$  with a much denser grid with millimeter steps thus providing a well-resolved image of the selected region. To meet this requirement for the non-contact setup, a very short acquisition time for each point is needed, thus causing a low CNR (related to the actual short pixel dwell time for a single pixel). Nevertheless, the small absorption changes corresponding to brain activation could be clearly detected in *in vivo* experiments since the contrast and the CNR for the depth of the cortex were still sufficient. This achievement was possible by block averaging of a number of repetitions of the stimulation paradigm and further spatial binning, both decreasing photon noise.

In conclusion, the non-contact setup, thanks to the fast-gated acquisition at a small source-detector distance, has several advantages. First of all, it has an improved dynamic range. Indeed, the dynamic range is about 4 decades higher than that of typical non-gated detectors, such as the PMTs used in fOXY. Unfortunately, the small active area of the

fast-gated detector (diameter  $100\ \mu\text{m}$ ) limits the system responsivity (see Table I). This parameter can be improved by using large-area sensors like silicon photomultipliers (SiPMs), which have been recently demonstrated in time-domain diffuse optics applications showing promising results.<sup>44,45</sup> However, to this purpose, a further research effort is required since the present SiPM technology does not allow the adoption of a time-gated detection scheme. The gating technique is a fundamental prerequisite to select and enhance the sensitivity for late photons that probe deeper regions. Indeed, hemoglobin concentration changes, for example, due to brain activation, occur in the cortex which is usually 1.5-2 cm below the scalp surface. The other main advantage provided by the higher and more symmetrical confinement of photons due to the small source-detector distance is the improved spatial resolution along the X direction. Indeed, the Y-resolution is similar for both setups but the X-resolution achievable with the non-contact setup is half compared to fOXY, thanks to the use of the 5 mm source-detector distance.

## VI. CONCLUSION

We have presented a novel setup based on a non-contact scanning approach and on a state-of-the-art high dynamic range detection based on a fast-gated SPAD module. This setup enables fast scanning (e.g., 1 frame/s) of an area of 34 mm by 40 mm with a dense array of points, thanks to the use of a short (few mm) source-detector distance.

The performances of the proposed setup were assessed using two standardized protocols specifically developed for time-domain optical brain imagers, the so-called BIP and nEUROPt protocols.<sup>29,30</sup>

The performances of our setup in terms of Y resolution are comparable with results obtained with other brain imagers, while other features such as CNR are affected by the small integration time when scanning images with a large number of pixels. The responsivity (on the order of  $10^{-5}\text{ mm}^2\text{ sr}$ ) is much smaller than that of other time-domain brain imagers (e.g., fOXY), mainly because of the non-contact optical imaging system and the small active area of the fast-gated detector. However, this is the only detector that nowadays can be efficiently fast-gated and is capable of tolerating the high intensity of early remitted photons. This is not trivial with other common detectors that can work in gated mode, such as PMTs or intensified CCD cameras. Indeed, these photocathode-based devices can experience a strong (yet not permanent) increase in the background noise when the cathode is exposed to strong illumination even when the electron-multiplication process is not active in the gate-off state.<sup>46</sup>

Furthermore, our approach introduces important advantages such as (i) the non-contact measurement scheme, useful in case of burn injuries, wounds, or difficult to treat subjects; (ii) the high dynamic range achievable, thanks to the fast-gating technique; (iii) a much better resolution along the X axis, due to the more confined region probed by the photons when using small source-detector distances of a few mm only. Those features enable an efficient detection of late photons (carrying information about structures buried up to 1.5 cm in depth) with an improved spatial resolution with respect

to brain imagers (e.g., fOXY) based on a typical interfiber distance of a few tens of mm. Another main advantage of the setup presented is the fast scanning approach that allows one to scan a wide area with a dense grid of points using only a single detector and with a frame time comparable to other diffuse optical imagers (typically 1 s), enabling dynamic measurements.

These advantages open the way to a new kind of brain imagers where monitoring of a larger area is done without any pain for the patient (due, for example, to pressure applied to gain a proper optical contact between the skin and the optode) and need for particular manipulation.

In the future, the development of novel devices for time-domain diffuse optics like low-cost and easily parallelizable pulsed laser sources and microelectronic fast-gated large-area detectors can strongly improve performances increasing both responsivity and penetration depth.<sup>44,47</sup>

## ACKNOWLEDGMENTS

This project has received funding from the European Union's Horizon 2020 research and innovation programme under Grant Agreement No. 654148 Laserlab-Europe. This work was partially supported by Cariplo Foundation under Grant No. 2013–0615.

- <sup>1</sup>A. Yodh and B. Chance, "Spectroscopy and imaging with diffusing light," *Phys. Today* **48**(3), 34–41 (1995).
- <sup>2</sup>A. Bellincontro, A. Taticchi, M. Servili, S. Esposito, D. Farinelli, and F. Mencarelli, "Feasible application of a portable NIR-AOTF tool for on-field prediction of phenolic compounds during the ripening of olives for oil production," *J. Agric. Food Chem.* **60**, 2665–2673 (2012).
- <sup>3</sup>I. Bargigia, A. Nevin, A. Farina, A. Pifferi, C. D'Andrea, M. Karlsson, P. Lundin, G. Somesfalean, and S. Svanberg, "Diffuse optical techniques applied to wood characterisation," *J. Near Infrared Spectrosc.* **21**, 259–268 (2013).
- <sup>4</sup>T. Durduran, R. Choe, W. B. Baker, and A. G. Yodh, "Diffuse optics for tissue monitoring and tomography," *Rep. Prog. Phys.* **73**, 076701 (2010).
- <sup>5</sup>P. Taroni, G. Quarto, A. Pifferi, F. Ieva, A. M. Paganoni, F. Abbate, N. Balestreri, S. Menna, E. Cassano, and R. Cubeddu, "Optical identification of subjects at high risk for developing breast cancer," *J. Biomed. Opt.* **18**, 060507 (2013).
- <sup>6</sup>D. Grosenick, K. T. Moesta, M. Möller, J. Mucke, H. Wabnitz, B. Gebauer, C. Stroszczynski, B. Wassermann, P. M. Schlag, and H. Rinneberg, "Time-domain scanning optical mammography: I. Recording and assessment of mammograms of 154 patients," *Phys. Med. Biol.* **50**, 2429–2449 (2005).
- <sup>7</sup>A. Pifferi, A. Torricelli, P. Taroni, A. Bassi, E. Chikoidze, E. Giambattistelli, and R. Cubeddu, "Optical biopsy of bone tissue: A step toward the diagnosis of bone pathologies," *J. Biomed. Opt.* **9**, 474–480 (2004).
- <sup>8</sup>L. Enfield, G. Cantanhede, M. Douek, V. Ramalingam, A. Purushotham, J. Hebden, and A. Gibson, "Monitoring the response to neoadjuvant hormone therapy for locally advanced breast cancer using three-dimensional time-resolved optical mammography," *J. Biomed. Opt.* **18**, 56012 (2013).
- <sup>9</sup>M. Ferrari and V. Quaresima, "A brief review on the history of human functional near-infrared spectroscopy (fNIRS) development and fields of application," *Neuroimage* **63**, 921–935 (2012).
- <sup>10</sup>D. R. Leff, O. J. Warren, L. C. Enfield, A. Gibson, T. Athanasiou, D. K. Patten, J. Hebden, G. Z. Yang, and A. Darzi, "Diffuse optical imaging of the healthy and diseased breast: A systematic review," *Breast Cancer Res. Treat.* **108**, 9–22 (2008).
- <sup>11</sup>D. A. Boas, C. E. Elwell, M. Ferrari, and G. Taga, "Twenty years of functional near-infrared spectroscopy: Introduction for the special issue," *Neuroimage* **85**(Part 1), 1–5 (2014).
- <sup>12</sup>M. A. Khalil, H. K. Kim, I.-K. Kim, M. Flexman, R. Dayal, G. Shrikhande, and A. H. Hielscher, "Dynamic diffuse optical tomography imaging of peripheral arterial disease," *Biomed. Opt. Express* **3**, 2288–2298 (2012).
- <sup>13</sup>O. Steinkellner, C. Gruber, H. Wabnitz, A. Jelzow, J. Steinbrink, J. B. Fiebach, R. Macdonald, and H. Obrig, "Optical bedside monitoring of cerebral perfusion: Technological and methodological advances applied in a study on acute ischemic stroke," *J. Biomed. Opt.* **15**, 61708–61710 (2010).
- <sup>14</sup>I. A. Nakhaeva, O. A. Zyuryukina, M. R. Mohammed, and Y. P. Sinichkin, "The effect of external mechanical compression on *in vivo* water content in human skin," *Opt. Spectrosc.* **118**, 834–840 (2015).
- <sup>15</sup>I. Sase, A. Takatsuki, J. Seki, T. Yanagida, and A. Seiyama, "Noncontact backscatter-mode near-infrared time-resolved imaging system: Preliminary study for functional brain mapping," *J. Biomed. Opt.* **11**, 054006 (2006).
- <sup>16</sup>T. Funane and A. Suzuki, "Noncontact brain activity measurement system based on near-infrared," *Appl. Phys. Lett.* **96**, 1–3 (2010).
- <sup>17</sup>D. Contini, L. Zucchelli, L. Spinelli, M. Caffini, R. Re, A. Pifferi, R. Cubeddu, and A. Torricelli, "Review: Brain and muscle near infrared spectroscopy/imaging techniques," *J. Near Infrared Spectrosc.* **20**, 15 (2012).
- <sup>18</sup>A. Puszcza, L. Di Sieno, A. Dalla Mora, A. Pifferi, D. Contini, A. Planat-Chrétien, A. Koenig, G. Boso, A. Tosi, L. Hervé, and J.-M. Dinten, "Spatial resolution in depth for time-resolved diffuse optical tomography using short source-detector separations," *Biomed. Opt. Express* **6**, 1–10 (2015).
- <sup>19</sup>A. Pifferi, A. Torricelli, L. Spinelli, D. Contini, R. Cubeddu, F. Martelli, G. Zaccanti, A. Tosi, A. Dalla Mora, F. Zappa, and S. Cova, "Time-resolved diffuse reflectance using small source-detector separation and fast single-photon gating," *Phys. Rev. Lett.* **100**, 138101 (2008).
- <sup>20</sup>G. Boso, A. Dalla Mora, A. Della Frera, and A. Tosi, "Fast-gating of single-photon avalanche diodes with 200 ps transitions and 30 ps timing jitter," *Sens. Actuators, A* **191**, 61–67 (2013).
- <sup>21</sup>A. Dalla Mora, A. Tosi, F. Zappa, S. Cova, D. Contini, A. Pifferi, L. Spinelli, A. Torricelli, and R. Cubeddu, "Fast-gated single-photon avalanche diode for wide dynamic range near infrared spectroscopy," *IEEE J. Sel. Top. Quantum Electron.* **16**, 1023–1030 (2010).
- <sup>22</sup>M. Mazurenka, A. Jelzow, H. Wabnitz, D. Contini, L. Spinelli, A. Pifferi, R. Cubeddu, A. Dalla Mora, A. Tosi, F. Zappa, and R. Macdonald, "Non-contact time-resolved diffuse reflectance imaging at null source-detector separation," *Opt. Express* **20**, 283–290 (2012).
- <sup>23</sup>M. Mazurenka, L. Di Sieno, G. Boso, D. Contini, A. Pifferi, A. Dalla Mora, A. Tosi, H. Wabnitz, and R. Macdonald, "Non-contact *in vivo* diffuse optical imaging using a time-gated scanning system," *Biomed. Opt. Express* **4**, 2257–2268 (2013).
- <sup>24</sup>H. Wabnitz, M. Mazurenka, L. Di Sieno, G. Boso, W. Becker, K. Fuchs, D. Contini, A. Dalla Mora, A. Tosi, R. Macdonald, and A. Pifferi, "Time-domain diffuse optical imaging of tissue by non-contact scanning," in *Advanced Time-Correlated Single Photon Counting Applications*, Springer I, Springer Series in Chemical Physics, edited by W. Becker (Springer International Publishing, 2015), Vol. 111, pp. 561–585.
- <sup>25</sup>V. Sankaran, M. J. Everett, D. J. Maitland, and J. T. Walsh, "Comparison of polarized-light propagation in biological tissue and phantoms," *Opt. Lett.* **24**, 1044–1046 (1999).
- <sup>26</sup>A. Dalla Mora, A. Tosi, D. Contini, L. Di Sieno, G. Boso, F. Villa, and A. Pifferi, "Memory effect in silicon time-gated single-photon avalanche diodes," *J. Appl. Phys.* **117**, 114501 (2015).
- <sup>27</sup>W. Becker, *The Bh TCSPC Handbook*, 6th ed. (Becker & Hickl, 2014).
- <sup>28</sup>W. Becker, *Advanced Time-Correlated Single Photon Counting Techniques* (Springer Science & Business Media, 2005), Vol. 81.
- <sup>29</sup>H. Wabnitz, D. R. Taubert, M. Mazurenka, O. Steinkellner, A. Jelzow, R. Macdonald, D. Milej, P. Sawosz, M. Kacprzak, A. Liebert, R. Cooper, J. Hebden, A. Pifferi, A. Farina, I. Bargigia, D. Contini, M. Caffini, L. Zucchelli, L. Spinelli, R. Cubeddu, and A. Torricelli, "Performance assessment of time-domain optical brain imagers. Part 1: Basic instrumental performance protocol," *J. Biomed. Opt.* **19**, 86010 (2014).
- <sup>30</sup>H. Wabnitz, A. Jelzow, M. Mazurenka, O. Steinkellner, R. Macdonald, D. Milej, N. Zolek, M. Kacprzak, P. Sawosz, R. Maniewski, A. Liebert, S. Magazov, J. Hebden, F. Martelli, P. Di Ninni, G. Zaccanti, A. Torricelli, D. Contini, R. Re, L. Zucchelli, L. Spinelli, R. Cubeddu, and A. Pifferi, "Performance assessment of time-domain optical brain imagers. Part 2: nEUROPT protocol," *J. Biomed. Opt.* **19**, 86012 (2014).
- <sup>31</sup>A. Dalla Mora, D. Contini, A. Pifferi, R. Cubeddu, A. Tosi, and F. Zappa, "Afterpulse-like noise limits dynamic range in time-gated applications of thin-junction silicon single-photon avalanche diode," *Appl. Phys. Lett.* **100**, 241111 (2012).
- <sup>32</sup>F. Martelli, A. Pifferi, D. Contini, L. Spinelli, A. Torricelli, H. Wabnitz, R. Macdonald, A. Sassaroli, and G. Zaccanti, "Phantoms for diffuse optical imaging based on totally absorbing objects. Part 1: Basic concepts," *J. Biomed. Opt.* **18**, 066014 (2013).
- <sup>33</sup>F. Martelli and G. Zaccanti, "Calibration of scattering and absorption properties of a liquid diffusive medium at NIR wavelengths. CW method," *Opt. Express* **15**, 486–500 (2007).

- <sup>34</sup>R. Michels, F. Foschum, and A. Kienle, "Optical properties of fat emulsions," *Opt. Express* **16**, 5907–5925 (2008).
- <sup>35</sup>L. Spinelli, F. Martelli, A. Farina, A. Pifferi, A. Torricelli, R. Cubeddu, and G. Zaccanti, "Calibration of scattering and absorption properties of a liquid diffusive medium at NIR wavelengths. Time-resolved method," *Opt. Express* **15**, 6589–6604 (2007).
- <sup>36</sup>L. Spinelli, M. Botwicz, N. Zolek, M. Kacprzak, D. Milej, P. Sawosz, A. Liebert, U. Weigel, T. Durduran, F. Foschum, A. Kienle, F. Baribeau, S. Leclair, J.-P. Bouchard, I. Noiseux, P. Gallant, O. Mermut, A. Farina, A. Pifferi, A. Torricelli, R. Cubeddu, H.-C. Ho, M. Mazurenka, H. Wabnitz, K. Klauenberg, O. Bodnar, C. Elster, M. Bénazech-Lavoué, Y. Bérubé-Lauzière, F. Lesage, D. Khoptyar, A. A. Subash, S. Andersson-Engels, P. Di Ninni, F. Martelli, and G. Zaccanti, "Determination of reference values for optical properties of liquid phantoms based on Intralipid and India ink," *Biomed. Opt. Express* **5**, 2037–2053 (2014).
- <sup>37</sup>F. Martelli, P. Di Ninni, G. Zaccanti, D. Contini, L. Spinelli, A. Torricelli, R. Cubeddu, H. Wabnitz, M. Mazurenka, R. Macdonald *et al.*, "Phantoms for diffuse optical imaging based on totally absorbing objects. Part 2: Experimental implementation," *J. Biomed. Opt.* **19**, 76011 (2014).
- <sup>38</sup>D. Contini, A. Dalla Mora, L. Spinelli, A. Farina, A. Torricelli, R. Cubeddu, F. Martelli, G. Zaccanti, A. Tosi, G. Boso, F. Zappa, and A. Pifferi, "Effects of time-gated detection in diffuse optical imaging at short source-detector separation," *J. Phys. D: Appl. Phys.* **48**, 45401 (2015).
- <sup>39</sup>A. Tosi, A. Dalla Mora, and F. Zappa, "All-silicon 1.55  $\mu\text{m}$  high-resolution photon counting and timing," *IEEE Photonics Technol. Lett.* **20**, 1956–1958 (2008).
- <sup>40</sup>D. Contini, A. Torricelli, A. Pifferi, L. Spinelli, F. Paglia, and R. Cubeddu, "Multi-channel time-resolved system for functional near infrared spectroscopy," *Opt. Express* **14**, 5418–5432 (2006).
- <sup>41</sup>D. Contini, L. Spinelli, M. Caffini, R. Cubeddu, and A. Torricelli, "A multichannel time-domain brain oximeter for clinical studies," *Proc. SPIE* **7369**, 73691D-1–73691D-6 (2009).
- <sup>42</sup>Hamamatsu Photonics K. K., "Photocathode technology," <http://www.hamamatsu.com/jp/en/technology/innovation/photocathode/index.html>.
- <sup>43</sup>A. Torricelli, A. Pifferi, L. Spinelli, R. Cubeddu, F. Martelli, S. Del Bianco, and G. Zaccanti, "Time-resolved reflectance at null source-detector separation: Improving contrast and resolution in diffuse optical imaging," *Phys. Rev. Lett.* **95**, 078101 (2005).
- <sup>44</sup>A. Dalla Mora, E. Martinenghi, D. Contini, A. Tosi, G. Boso, T. Durduran, S. Arridge, F. Martelli, A. Farina, A. Torricelli, and A. Pifferi, "Fast silicon photomultiplier improves signal harvesting and reduces complexity in time-domain diffuse optics," *Opt. Express* **23**, 13937–13946 (2015).
- <sup>45</sup>E. Martinenghi, A. Dalla Mora, D. Contini, A. Farina, F. Villa, A. Torricelli, and A. Pifferi, "Spectrally resolved single-photon timing of silicon photomultipliers for time-domain diffuse spectroscopy," *IEEE Photonics J.* **7**, 6802512 (2015).
- <sup>46</sup>S.-O. Flyckt and C. Marmonier, *Photomultiplier Tubes: Principles and Applications* (Photonis, 2002).
- <sup>47</sup>A. Dalla Mora, D. Contini, S. Arridge, F. Martelli, A. Tosi, G. Boso, A. Farina, T. Durduran, E. Martinenghi, A. Torricelli, and A. Pifferi, "Towards next-generation time-domain diffuse optics for extreme depth penetration and sensitivity," *Biomed. Opt. Express* **6**, 1749–1760 (2015).